The Multidecadal Variability of the Asymmetric Mode of the Boreal Autumn Hadley Circulation and Its Link to the Atlantic Multidecadal Oscillation

YIPENG GUO

State Key Laboratory of Numerical Modeling for Atmospheric Sciences and Geophysical Fluid Dynamics, Institute of Atmospheric Physics, Chinese Academy of Sciences, and College of Earth Science, University of Chinese Academy of Sciences, Beijing, China

JIANPING LI, JUAN FENG, FEI XIE, AND CHENG SUN

College of Global Change and Earth System Science, Beijing Normal University, and Joint Center for Global Change Studies, Beijing, China

JIAYU ZHENG

State Key Laboratory of Satellite Ocean Environment Dynamics, Second Institute of Oceanography, Hangzhou, China

(Manuscript received 6 January 2015, in final form 18 December 2015)

ABSTRACT

Previous studies show that the first principal mode of the variability of the seasonal mean Hadley circulation (HC) is an equatorial asymmetric mode (AM) with long-term trend. This study demonstrates that the variability of the boreal autumn [September–November (SON)] HC is also dominated by an AM, but with multidecadal variability. The SON AM has ascending and descending branches located at approximately 20°N and 20°S, respectively, and explains about 40% of the total variance. Further analysis reveals that the AM is closely linked to the Atlantic multidecadal oscillation (AMO), which is associated with a large cross-equatorial sea surface temperature (SST) gradient and sea level pressure (SLP) gradient. The cross-equatorial thermal contrast further induces an equatorial asymmetric HC anomaly. Numerical simulations conducted on an atmospheric general circulation model also suggest that AMO-associated SST anomalies can also induce a cross-equatorial SLP gradient and anomalous vertical shear of the meridional wind at the equator, both of which indicate asymmetric HC anomaly. Therefore, the AM of the variability of the boreal autumn HC has close links to the AMO. Further analysis demonstrates that the AMO in SON has a closer relationship with AM than those in the other seasons. A possible reason is that the AMO-associated zonal mean SST anomaly in the tropics has differences among the four seasons, which leads to different atmospheric circulation responses.

The AM in SON has inversed impacts on the tropical precipitation, suggesting that the precipitation difference between the northern and southern tropics has multidecadal variability.

1. Introduction

The Hadley circulation (HC) is a large-scale thermally driven atmospheric circulation, rising in the deep tropics and sinking in the subtropics (Held and Hou 1980). It transports momentum and heat from low to high latitudes and converges water vapor from the subtropics to the deep tropics. As a result, the HC has remarkable impacts on both tropical and extratropical climates (e.g., Lindzen 1994; Hou 1998; Chang 1995; Diaz and Bradley 2004).

Given the importance of the HC, many studies focused on the long-term changes of the HC strength and width. Chen et al. (2002) and Wielicki et al. (2002) found that the HC strengthened between 1985 and 2000 by analyzing the solar flux and radiation budgets. Quan et al. (2004) also reported an intensification of the boreal winter [December–February (DJF)] HC since the 1950s. Similar results were reported by Ma and Li

Denotes Open Access content.

Corresponding author address: Dr. Jianping Li, College of Global Change and Earth System Science, Beijing Normal University, No. 19, XinJieKouWai St., Beijing 100875, China.
E-mail: ljp@bnu.edu.cn

DOI: 10.1175/JCLI-D-15-0025.1

(2007, 2008), Mitas and Clement (2005), and Hu et al. (2005). However, the long-term change of the HC strength has uncertainties in boreal summer [June–August (JJA)]. Some studies remarked that the HC strength has minor changes in JJA (e.g., Tanaka et al. 2004; Mitas and Clement 2006; Sun and Zhou 2014), whereas Feng et al. (2011) argued that the boreal summer HC has been weakened. Zhao and Moore (2008) also reported a decreasing trend in the regional meridional circulation over Asia and Africa. On the other hand, Fu et al. (2006) reported that the HC boundary shifted poleward by approximately 2° latitude during the period of 1979–2005, indicating an expansion of the HC. Hu and Fu (2007) found that the HC expansion primarily occurs in boreal summer and autumn seasons. Some studies further explored the HC expansion by comparing general circulation model (GCM) simulation results and observations, attempting to figure out the causes of the expansion (e.g., Frierson et al. 2007; Lu et al. 2007; Johanson and Fu 2009).

The principal modes of the variability of the HC are also intensively studied. Dima and Wallace (2003) investigated the annual march of the climatological mean HC and found it is dominated by two components: a solstitial cell varying sinusoidally and seasonally, with rising (descending) motion in the summer (winter) hemisphere, and a seasonally invariant pair of cells, with rising (descending) motion at the equator (subtropics). Ma and Li (2008) investigated the principal modes of the year-to-year variability of the DJF HC, showing that the first principal mode (EOF 1) is asymmetric about the equator (asymmetric mode) and the second principal mode (EOF 2) is symmetric about the equator (symmetric mode). The asymmetric mode (AM) displays a long-term upward trend, while the symmetric mode (SM) exhibits interannual variability. The AM and SM also exist in the boreal summer (Feng et al. 2011) and spring [March–May (MAM)] (Feng et al. 2013). The AM and SM in MAM and JJA also display a long-term trend and interannual variability, respectively.

The AM encompasses cross-equatorial low-level wind (e.g., Feng and Li 2013), which burdens energy transport across the equator and influences the tropical precipitation (e.g., Friedman et al. 2013; Donohoe et al. 2014). The AM is a solstitial cell with a cross-equatorial mean meridional circulation anomaly, as depicted by Dima and Wallace (2003). The mean meridional circulation is sensitive to the meridional sea surface temperature (SST) gradient (e.g., Feng et al. 2013; Hu et al. 2014; Zhan et al. 2013). More generally, as reviewed by Chiang and Friedman (2012), any factors that cause interhemispheric thermal contrast could induce meridionally asymmetric circulation anomaly.

The tropical SST anomaly (SSTA) patterns are important to the interhemispheric thermal contrast. Feng et al. (2013) pointed out that the AM in MAM shows long-term trend because the southern tropical ocean warms faster than the northern tropics. A GCM study by Mantsis and Clement (2009) showed that there is a multidecadal signal in the annual mean cross-equatorial circulation, which is associated with the interhemispheric SST difference. Sun et al. (2013) pointed out that the EOF-3 mode of the zonally averaged SSTA presents an interhemispheric dipole mode that has multidecadal variability. They further suggested that the interhemispheric dipole mode is critical to the cross-equatorial wind.

Given that the AM is closely linked with the cross-equatorial thermal gradient, it is an interesting question whether the AM has multidecadal variability. The multidecadal signal exists in the annual mean cross-equatorial circulation (e.g., Mantsis and Clement 2009), while the previous studies proved that the AMs of the variability of the boreal spring (Feng et al. 2013), summer (Feng et al. 2011), and winter (Ma and Li 2008) HCs have long-term trends. Is it possible that there exists a multidecadal signal in the principal modes of the variability of the boreal autumn [September–November (SON)] HC? Most previous studies have focused on the HC variability in solstitial seasons (e.g., Ma and Li 2008; Feng et al. 2011; Tanaka et al. 2004; Mitas and Clement 2005; Quan et al. 2004); however, the study by Feng et al. (2013) drew attention to the equinoctial season. It is necessary to investigate the principal modes of the HC variability in SON, which is rarely addressed in previous studies. Is the SON HC variability also dominated by the AM? If so, how does it change?

The primary goal of this study is to explore the spatial and temporal characteristics of the principal modes of the variability of the SON HC, the relationship with the SSTA, and the potential climate impacts. The remainder of the manuscript is arranged as follows: Section 2 describes the data sources and methodologies employed in this paper. Section 3 presents the spatial and temporal characteristics of the principal modes of the variability of the SON HC. Links between the principal modes and the SSTA are shown in section 4. Section 5 presents numerical simulations to further support observational results. Section 6 discusses the potential impacts of the principal modes of the SON HC variability on the tropical precipitation. Finally, a summary and discussion are presented in section 7.

2. Datasets and methodology

a. Observational datasets

The reanalysis datasets of the atmospheric fields used in this study include the following:

1) National Centers for Environmental Prediction (NCEP)–National Center for Atmospheric Research (NCAR) reanalysis (NCEP-1); the horizontal resolution is 2.5° × 2.5° with 17 vertical levels, covering the period from 1948 to the present (Kalnay et al. 1996).
2) The Twentieth Century Reanalysis (20CR) data, which have a horizontal resolution of 2° × 2° and 24 vertical levels, covering the period from 1871 to 2010 (Compo et al. 2011).
3) NCEP–Department of Energy (DOE) Atmospheric Model Intercomparison Project (AMIP)-II Reanalysis (NCEP-2) data, which covers the period from 1979 to the present, with a horizontal resolution of 2.5° × 2.5° and 17 vertical levels (Kanamitsu et al. 2002).
4) Japanese 25-Year Reanalysis data (JRA-25; Onogi et al. 2005), based on a 2.5° × 2.5° latitude–longitude grid with 23 vertical levels.
5) NCEP Climate Forecast System Reanalysis (CFSR) dataset from 1979 to the present, which has a horizontal resolution of 2.5° × 2.5° with 37 vertical levels (Saha et al. 2010).
6) The 40-yr European Centre for Medium-Range Weather Forecasts (ECMWF) Re-Analysis (ERA-40) data from 1957 to 2002, which have a horizontal resolution of 2.5° × 2.5° with 23 vertical levels (Uppala et al. 2005).
7) ECMWF interim reanalysis (ERA-Interim, hereafter ERAI) data from 1979 to 2008, which have a 1° × 1° horizontal resolution and 37 vertical layers (Dee et al. 2011).
8) Modern-Era Retrospective Analysis for Research and Applications (MERRA) reanalysis dataset for 1979–2012. The MERRA dataset has a horizontal resolution of 1.25° × 1.25° with 37 vertical layers from 1000 hPa to 1 hPa (Rienecker et al. 2011).

The SST data are from the Extended Reconstructed SST version 3b dataset (ERSST V3b; Smith et al. 2008), which covers the period from 1854 to present and has a horizontal resolution of 2° × 2°. The global land precipitation data are from the Climate Research Unit (CRU) dataset, covering the period of 1901–2011 with horizontal resolution of 0.5° × 0.5° (Mitchell and Jones 2005).

We also used the model data of AMIP simulations for the phase 5 of the Coupled Model Intercomparison Project (CMIP5), which can provide more evidence to support the reanalyses. Three models (CanAM4, IPSL-CM5A-MR, and GISS-E2-R) are chosen because they have time coverage from 1950 to near present. Models with multiple runs are averaged over all runs.

b. Methodology

The meridional streamfunction (MSF) is used to characterize the HC. It is calculated by vertically integrating the zonal mean meridional wind (Holton 1992; Li 2001). Positive (negative) MSF values indicate a clockwise (anticlockwise) circulation. The MSF is defined as

$$\psi = \int \frac{2\pi R \cos\phi}{g} [\overline{v}]\, dp, \tag{1}$$

where $[\overline{v}]$ is the zonal mean meridional wind, R is the radius of Earth, ϕ is the latitude, g is the acceleration due to gravity, and p is atmospheric pressure. The overbar and brackets indicate the temporal and zonal mean, respectively. The interval of the integral is from 10 hPa to the surface.

The differences in zonal mean meridional winds between 850 and 200 hPa are used to represent the HC strength (e.g., Feng et al. 2013). The empirical orthogonal function (EOF) analysis is used to extract the principal modes of the year-to-year variability of the HC.

c. Model description

In this study we used an atmospheric GCM, the Community Atmosphere Model version 5.0 (CAM5), to further explore the underlying mechanisms involved in HC variability. CAM5 is the atmospheric component of the Community Earth System Model (CESM), and it has 30 vertical layers from the surface to 2.25 hPa. All simulations performed as part of this work were performed at a horizontal resolution of 1.9° × 2.5°.

3. Principal modes of the variability of the boreal autumn HC

Figure 1 shows the climatology and the first two principal modes of the SON HC during the period of 1979–2010. The SON climatological MSF displays consistent spatial patterns among the different reanalysis datasets. It has two cells sharing a common ascending branch at approximately 10°N, and the descending branches of the two cells are at approximately 30°S and 30°N, respectively. Although different reanalyses show consistent spatial structure of the climatological HC, they still have discrepancies in strength. For the

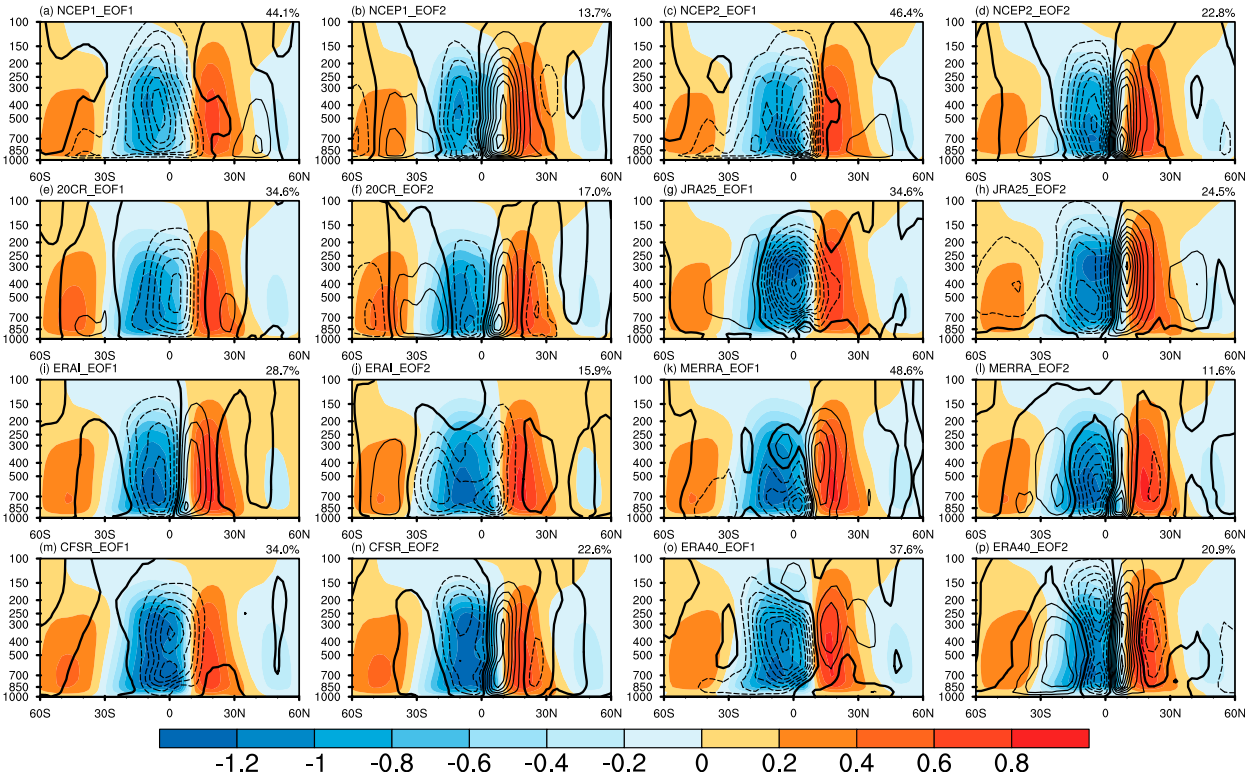

FIG. 1. Climatology (shading, unit: 1.0×10^{11} kg s^{-1}) and the first two principal modes (contour) of SON MSF during the period of 1979–2010 based on the (a),(b) NCEP-1, (c),(d) NCEP-2, (e),(f) 20CR, (g),(h) JRA-25, (i),(j) ERAI, (k),(l) MERRA, (m),(n) CFSR, and (o),(p) ERA-40 data. The EOF-1 (EOF-2) modes are shown in the first and third (second and fourth) columns. Contour interval is 0.02. The solid (dashed) lines represent the positive (negative) values.

southern cells, NCEP-1 is the weakest while JRA-25 is the strongest. All reanalyses have relatively equivalent strength for the northern cells.

For the AM, the circulation centers are confined between 15°S and 15°N for all datasets, indicating an anticlockwise cell assuming the PC is positive. But discrepancies exist in both strength and spatial structure. NCEP-1 and NCEP-2 extend their main bodies to about 30°S, while 20CR and JRA-25 present a quite weak clockwise cell over 20°–40°S. In Northern Hemisphere (NH), there also exist clockwise cells next to the main body for all the datasets except for JRA-25, which extends its main body to the high latitudes. It is worth noting that the AMs of the SON and MAM HC variability are different. The AM in SON has a much wider latitudinal extent, covering approximately 40° of latitude, while it only covers 30° of latitude in MAM (Feng et al. 2013). This difference may lead to different climatic impacts in the extratropics in these two seasons.

The SM has two cells located at the flanks of the equator, which have comparable magnitudes with opposite signs. The SMs account for 13.7% to 30.5% of the total variance and cover the latitude band 15°S–15°N, while only JRA-25 extends both of its two cells to the high latitudes; thus one should be cautious when using the JRA-25 to analyze the SM. The relative strengths of the two cells from NCEP-1 and 20CR are different from those of the other reanalyses. The former shows much stronger northern cells than southern cells, while the latter shows comparable strengths of the two cells.

One of the main differences of the first two principal modes between ERAI and the other reanalyses is the sequence of AM and SM. PC1 of ERAI has high (low) correlation coefficients, $R > 0.58$ ($R < 0.55$), with the PC2 (PC1) of the other reanalyses. Similarly, the EOF-1 mode of ERAI has high (low) pattern correlation coefficients with the EOF-2 (EOF-1) modes of the other datasets: R ranges from 0.68 to 0.96 (0.08 to 0.68). This indicates that the EOF-1 mode of ERAI is SM, which occurs as EOF-2 modes in the other reanalyses.

Another important difference is that the EOF-1 modes of MERRA and ERA-40 present anomalous cells accompanied with the main body of AM in the Northern Hemisphere, which does not occur in the other reanalyses (Figs. 1k,o). The PC1s of MERRA and ERA-40 have linear trends of 0.1 and 0.12 standard deviations

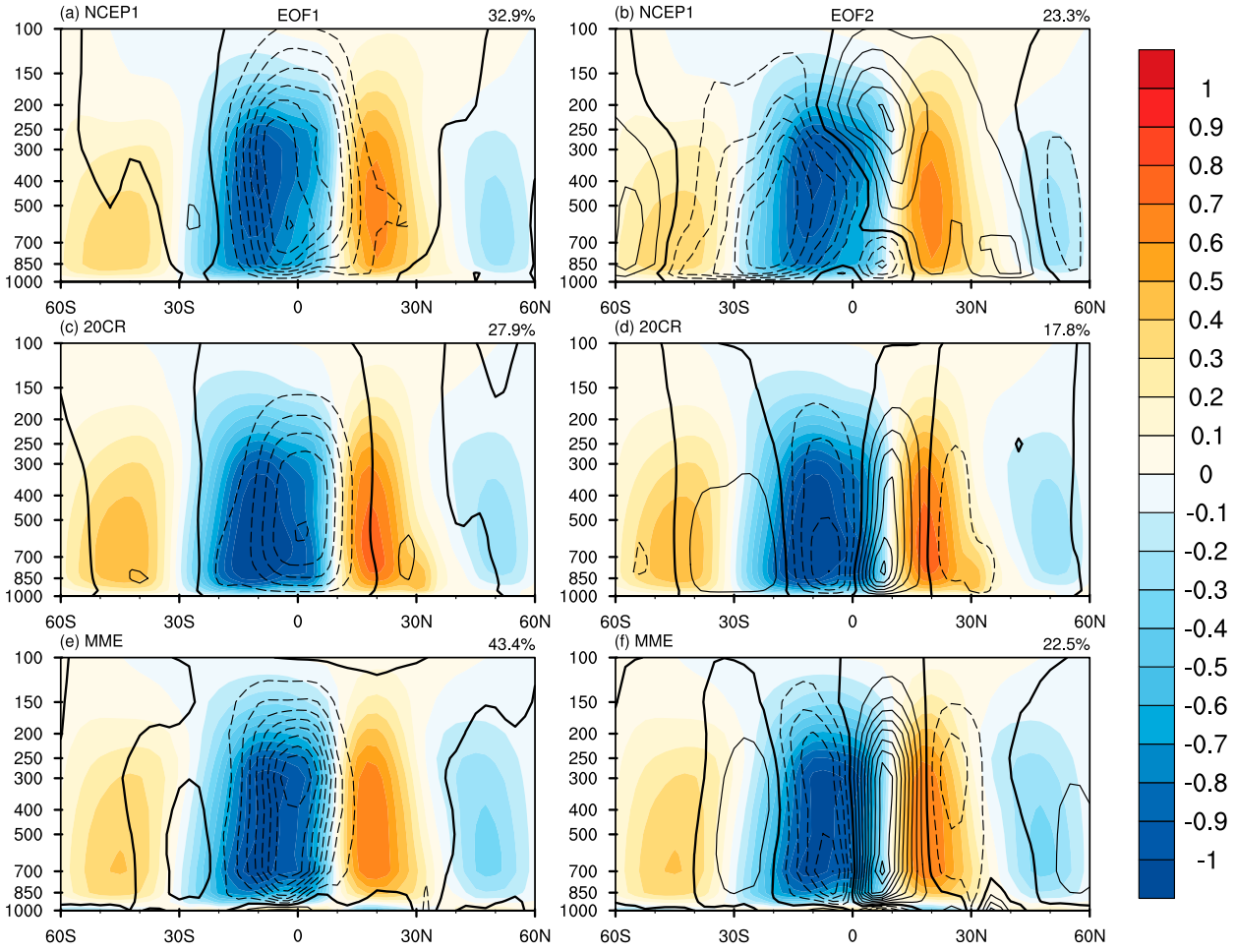

FIG. 2. As in Fig. 1, but for (a),(b) NCEP-1, (c),(d) 20CR, and (e),(f) a multimodel (CanAM4, IPSL-CM5A-MR, and GISS-E2-R) ensemble mean. Periods for NCEP-1 and 20CR are 1950–2010; for the ensemble mean, it is 1950–2009.

per year, respectively, indicating that the anomalous cells have strengthening trends. As the climatological HC in SON has two cells with comparable strength on each side of the equator, we checked the intensity change of northern cell of each datasets. The northern cells of MERRA and ERA-40 show changes of 1.23% and 0.81% yr^{-1}, respectively, while other datasets only shows small changes ranging from −0.18% to 0.43% yr^{-1}, much smaller than those of MERRA and ERA-40. The results indicate that the anomalous cells over the Northern Hemisphere in EOF-1 modes of MERRA and ERA-40 are possibly induced by strengthening trends of the northern cell of the HC in SON. Mitas and Clement (2006) pointed out that the strengthening trend of HC may be artificial because of the instrumental system biases of the radiosonde observation (Santer et al. 2005). The radiosonde observation data may damp the temperature trends at middle to high levels in the tropical troposphere, which leads to a biased lapse rate and induces the artificial strengthening trends of the HC. By comparing reanalyses and model outputs, Feng et al. (2011) suggested that the trend of HC in JJA for ERA-40 may be artificial. Held and Soden (2006) suggested that the tropical circulation would be weakened rather than strengthened in response to global warming. Thus, the strengthening trends of the HC should be treated with caution. Among the eight reanalyses, only ERA-40 and MERRA show an anomalous cell in the Northern Hemisphere (Figs. 1k,o). The strengthening trends in MERRA and ERA-40 may be artificial given the study of Mitas and Clement (2006), but further investigation is needed to verify the results.

The above results are based on the period of 1979–2010. In this study, we focus on the HC multidecadal variability. Figure 2 is the same as in Fig. 1, but with different time coverage. The period for NCEP-1 and 20CR is 1950–2010, while 1950–2009 is used for the multimodel ensemble (MME) mean. The linear trends

are removed in order to explore the multidecadal signal. The climatological HC during the period of 1950–2010 (1950–2009 for the MME) has consistent spatial structure among different datasets. EOF-1 modes of all the three datasets show the AM, accounting for 32.9% (NCEP-1), 27.9% (20CR), 44.0% (MME) of the total variance. EOF-2 modes are SM for the three datasets, but the SM of NCEP-1 has much larger latitude coverage than those of 20CR and MME. The biases of the SM will not be discussed here because we mainly focus on the AM, which is more consistent in spatial structure among the different datasets.

Figures 3a–c show the time series of the first principal modes shown in Fig. 2. For the sake of convenience, the time series of the AM is defined as the asymmetric mode index (AMI). For the three datasets, the AMI presents a positive phase from 1950 to 1970, followed by a negative phase from 1970 to the 1990s, and then returns to a positive phase after the 1990s, indicating multidecadal variability, which can be more easily observed via the 11-yr running mean (Figs. 3a–c; indicated by red dashed curves). The correlation coefficients of the AMI among the three datasets are above 0.37, significant at 95% confidence level when using a two-tailed Student's *t* test with the effective number of degrees of freedom (e.g., Li et al. 2012), which implies good consistency among different datasets. However, NCEP-1 shows larger amplitude of the multidecadal variability than the other two datasets, suggesting that uncertainty exists in the magnitude of the multidecadal variability.

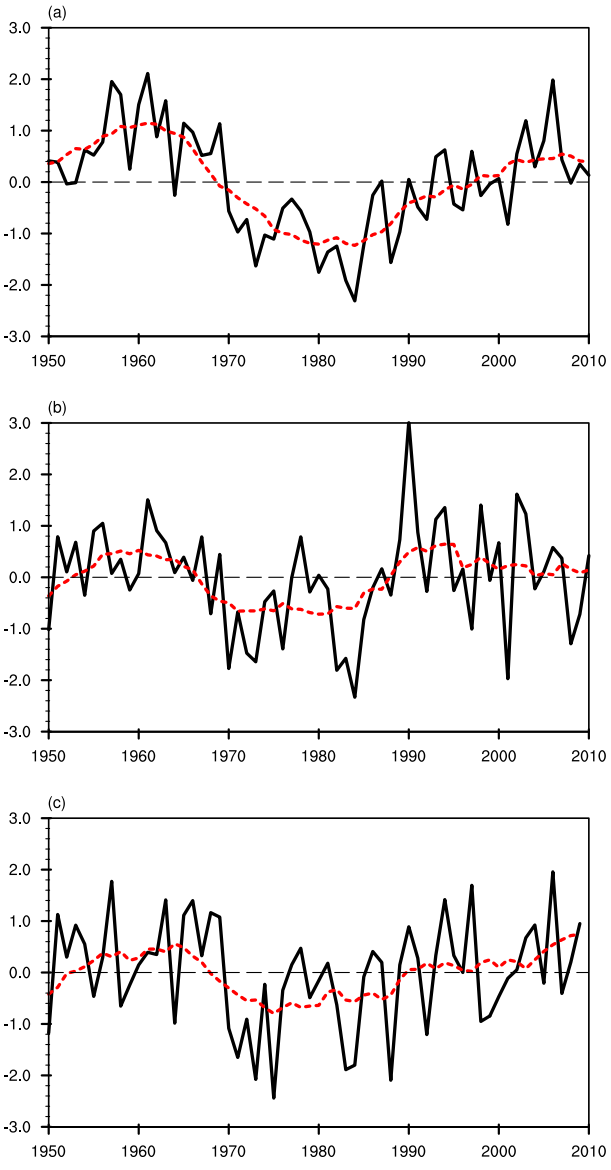

FIG. 3. The time series of AMI (solid lines) of the SON HC from (a) NCEP-1, (b) 20CR, and (c) the multimodel ensemble mean. Red dashed curves are 11-yr running means of the AMI. The time period is 1950–2010 for NCEP-1 and 20CR and 1950–2009 for the ensemble mean.

4. Links between SST and the AM of the SON HC variability

To explore the connection between the multidecadal variability of the AM and the SST, Fig. 4a shows the correlation map between the AMI and the SSTA. The correlation coefficients display an interhemispheric dipole pattern, with positive (negative) correlation over most of the Northern (Southern) Hemisphere oceans, which implies that the relationship between the AMI and the SSTA has robust interhemispheric contrast. The correlation pattern is quite similar to the Atlantic multidecadal oscillation (AMO) pattern (Fig. 4b; Parker et al. 2007), which is also closely associated with the EOF-3 of the global SSTA. Figure 4c shows the evolution of the AMI, the detrended AMO index (AMOI)—defined as the area-averaged SSTA over the North Atlantic (0°–70°N, 95°W–30°E) (Knight et al. 2005)—and the PC3 of the global SSTA. The AMI has a close relationship with the AMOI, with a correlation coefficient of 0.57, which is significant at a 99.9% confidence level (Table 1). According to Sun et al. (2013) the EOF-3 of the zonal mean SSTA represents an interhemispheric dipole mode that is closely associated with the AMO. Mantsis and Clement (2009) documented that the multidecadal signal observed in the variability of the annual mean HC is related to the variability of the interhemispheric SST difference.

To further determine whether the AMO can lead to an AM-like circulation anomaly, Fig. 5 shows composite differences in the MSF, vertical velocity, zonal mean meridional wind, and mean meridional wind shear

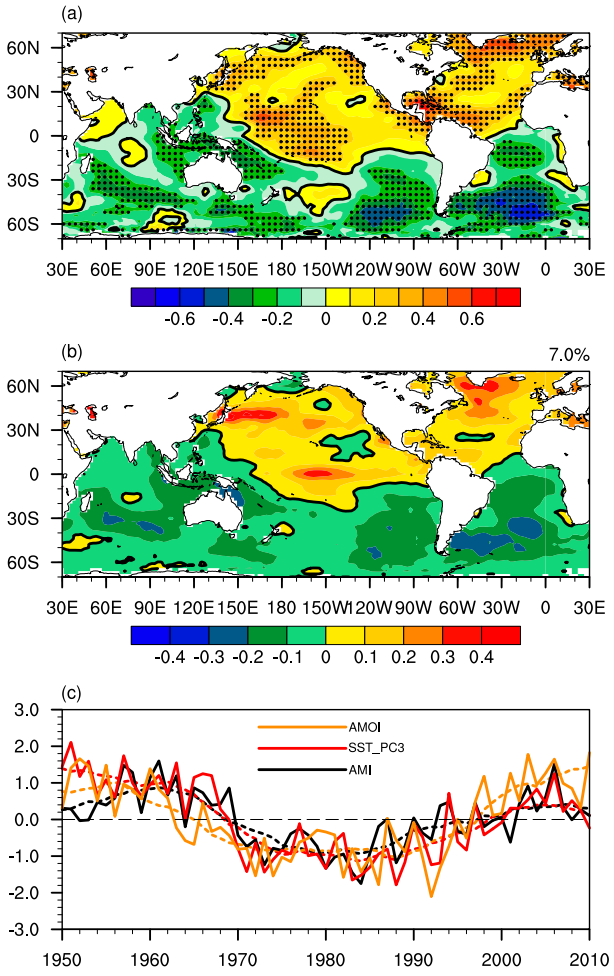

FIG. 4. (a) Correlation map between the AMI and global SSTA for 1950–2010. The black contours denote the zero line. The stippling indicates significance is at the 90% confidence level. (b) EOF-3 mode of the global SSTA. (c) Time series of the standardized AMI (black curve), the AMOI (yellow curve) and the PC3 of the SSTA (red curve). Dashed lines denote the 11-yr running means.

between 850 and 200 hPa based on the positive (AMOI greater than one standard deviation) and negative (AMOI less than one negative standard deviation) AMO phases. The composite difference of the MSF (Fig. 5a) shows an asymmetric structure, which resembles the AM, with a rising branch at 20°N and sinking branch at 20°S. The main body of the composite MSF anomaly is significant at 95% confidence level.

The composite difference of the vertical velocity (Fig. 5b) matches well with the composite MSF (Fig. 5a), with strong ascending (descending) motion over 5°–20°N (5°S–5°N). Nevertheless, the descending motion extends to the Northern Hemisphere and still indicates a solstitial pattern. The anomalous cell core may be located several degrees of latitude away from the equator;

TABLE 1. Correlation coefficients between the AMI and the MASI, detrended MASI, and AMOI during the four seasons, respectively. Values in bold exceed a 99% confidence level.

	MAM	JJA	SON	DJF
MASI	**0.72**	**0.53**	**0.59**	**0.61**
MASI_detrend	0.29	0.22	**0.56**	0.19
AMOI	0.03	0.27	**0.57**	0.07

its location depends largely on the displacement of the thermal equator (e.g., Dima and Wallace 2003), which may be determined by the location of the underlying heating center (e.g., Lindzen and Hou 1988).

Figure 5c shows the composite difference of the zonal mean meridional wind, which is strongly southerly in the lower troposphere and northerly over the upper troposphere, constituting a conspicuous cross-equatorial circulation anomaly. Figure 5d shows composites of the zonal mean meridional wind shear between 850 and 200 hPa based on positive and negative AMO phases. The wind shear is reversed between the two phases, implying that the positive and negative phases of the AMO can induce opposite asymmetric circulation anomalies. These results indicate a close relationship between the AMO and the AM in SON.

To further demonstrate that the above composite results do not depend on the methods, Fig. 6 shows regression patterns of the MSF and vertical velocity with respect to the AMOI. The regressed MSF (Fig. 6a) shows a similar pattern to that of the composite difference (Fig. 5a). The regressed vertical velocity also displays a matchable pattern associated with the regressed MSF (Fig. 6b), with rising and descending motions located over the north and south of the equator, respectively, constituting an asymmetric circulation anomaly.

The above analysis demonstrates that the occurrence of the AMO can induce asymmetric circulation anomaly. However, the correlation map between the AMI and the SSTA presents a global pattern (Fig. 4a), indicating that the AMO may be not the only factor that can induce an asymmetric circulation anomaly. To evaluate the roles of the interhemispheric SST difference over different ocean basins, a composite analysis is performed based on the meridional asymmetric SST index (MASI) of each ocean basin. The MASI is defined as (Feng and Li 2013)

$$\mathrm{MASI} = \mathrm{SSTA}_{(5°–15°\mathrm{N})} - \mathrm{SSTA}_{(15°–5°\mathrm{S})}, \qquad (2)$$

where the SSTA can be either a zonal or regional mean. The global ocean is divided into three sectors: the Indian Ocean (40°–110°E), the Pacific Ocean (120°E–90°W), and the Atlantic Ocean (10°–60°W).

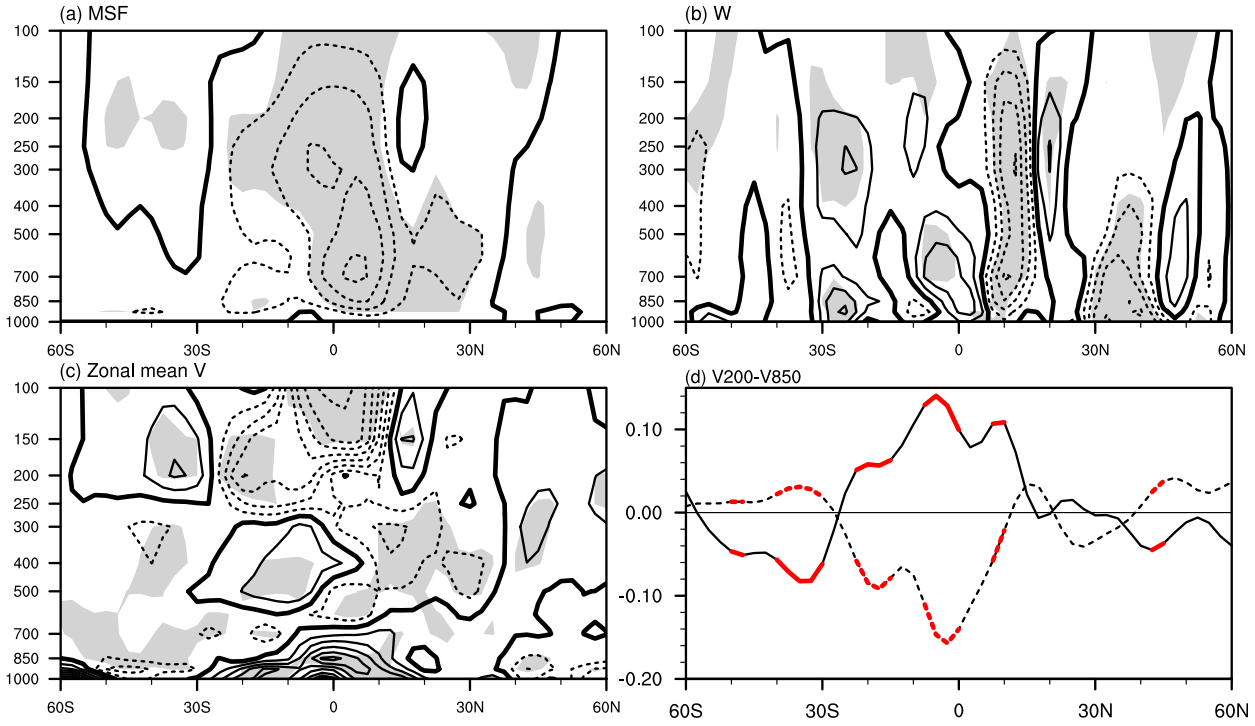

FIG. 5. Composite differences of (a) the MSF (10^{10} kg s^{-1}), (b) zonal mean vertical velocity (Pa s^{-1}), and (c) zonal mean meridional wind (m s^{-1}). The contour intervals are 0.2 × 10^{10} kg s^{-1} for (a), 0.5 × 10^{-3} Pa s^{-1} for (b), and 0.04 m s^{-1} for (c). Shading indicates significance at the 90% confidence level. (d) Composites of the positive (solid line) and negative (dashed line) zonal mean meridional wind shear (m s^{-1}) between 200 and 850 hPa, based on the positive and negative AMO phases. The line highlighted by red color indicates exceeding 90% confidence level.

Figure 7 shows the linear regression of the MSF and vertical velocity with respect to the MASI over the Indian Ocean, Pacific Ocean, and Atlantic Ocean sectors, respectively. The regressed MSF based on the Atlantic MASI (Fig. 7a) shows an equatorially asymmetric pattern, with a rising (descending) branch over 10°–20°N (10°–20°S). The main body of the regressed cell is significant at 95% confidence level (gray shading). The structure is similar to the AM and the composite difference of the MSF based on the AMOI (Figs. 5a and 6a). The regressed vertical velocity (Fig. 7d) shows rising and sinking motions over the flanks of the equator, matching the structure of the MSF.

However, no significant asymmetric pattern was found for the MSF regressed with respect to the Pacific MASI. Although the regressed MSF exhibits an asymmetric structure over the middle and high troposphere, only that over the Northern Hemisphere is statistically significant (Fig. 7b). The regressed vertical velocity shows upward (downward) motion at the equator (over the flanks of the equator), indicating a symmetric circulation anomaly (Fig. 7e). The regressed MSF pattern with respect to the Indian Ocean MASI also presents a symmetric pattern, with clockwise and anticlockwise cells located at the north and south of the equator (Fig. 7c). The corresponding regressed vertical velocity shows strong upward motion at the equator and downward motions over 10°–20°S and 10°–20°N, respectively.

The above analysis implies that the Atlantic Ocean is more related to the cross-equatorial circulation anomaly than the other two ocean basins. Thus, the AMO-related Atlantic MASI is crucial to the occurrence of the asymmetric circulation anomaly, indicating that the AMO may play a major role in the AM formation.

To illustrate how AMO induces cross-equatorial circulation anomaly, Fig. 8 shows the regression patterns of the zonally averaged SSTA, sea level pressure (SLP), vertical velocity at 500 hPa (w500), and meridional wind at 850 hPa (V850) and 100 hPa (V100), with respect to the AMOI. The regressed zonal mean SSTA (Fig. 8a) shows an obvious SST gradient across the equator, although the magnitude of the SSTA itself is not significant at a 90% confidence level. Yet, the corresponding SLP anomaly shows a significant cross-equatorial gradient (Fig. 8b). The regressed w500 indicates strong ascending (descending) motion over the northern (southern) tropics (Fig. 8c). Correspondingly, the regressed V850

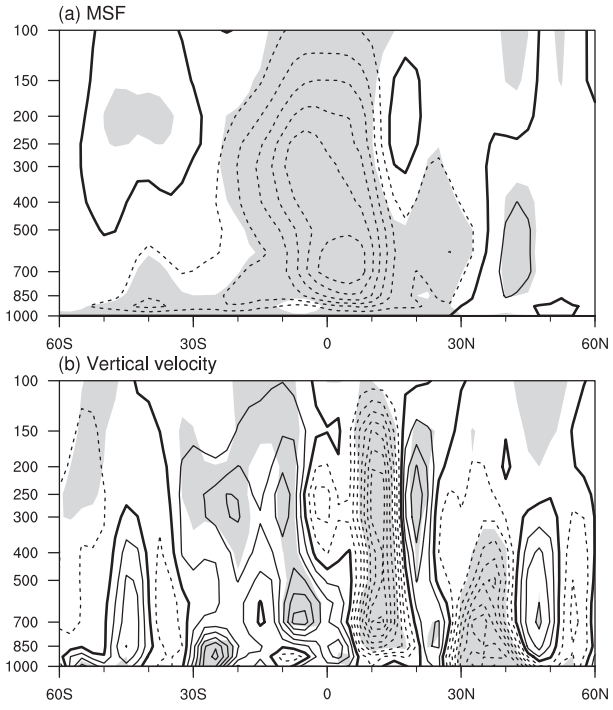

FIG. 6. Regression patterns of the (a) MSF and (b) vertical velocity with respect to the AMOI. Shading indicates significance at the 90% confidence level.

shows strong southerlies in the lower troposphere, while V100 shows strong northerlies in the upper troposphere across the equator (Fig. 8d), indicating a robust cross-equatorial circulation anomaly. The meridional wind anomalies are all statistically significant at a 90% confidence level.

5. Model simulation results

To further support the observational results, we performed five experiments with CAM5. The monthly observed SST and sea ice fields are from the United Kingdom Meteorological Office Hadley Centre for Climate Prediction and Research. The SST used in the control experiment (E1) is the monthly mean climatological SST based on the period of 1950–2010, which has only an annual cycle without year-to-year variability. In the four sensitivity experiments (E2–E5) the SST is as in E1, but other changes are made as follows: E2 was perturbed with AMO-associated SSTA; in E3, only the Atlantic Ocean (90°S–90°N, 80°W–30°E) was perturbed with AMO-associated SSTA; in E4, only the Pacific Ocean (90°S–90°N, 160°E–80°W) was perturbed with the AMO-associated SSTA; and in E5, only the Indian Ocean (90°S–90°N, 40°–160°E) was perturbed with the AMO-associated SSTA. In the sensitivity experiments, the SST perturbation was only exerted in SON. The AMO-associated SSTA is the composite SSTA difference between the positive (AMOI greater than one standard deviation) and negative (AMOI less than one negative standard deviation) AMO phases during the boreal autumn from 1950 to 2010. All the experiments were run for 35 continuous years, with the first five years used as the model spinup and the remaining 30 years of model outputs used for analysis. The analysis of the model results is based on the mean of the 30 model years.

Figure 9a shows the climatological MSF and the zonal mean vertical velocity in E1. The MSF shows similar spatial patterns to those in observations (Fig. 2), with the

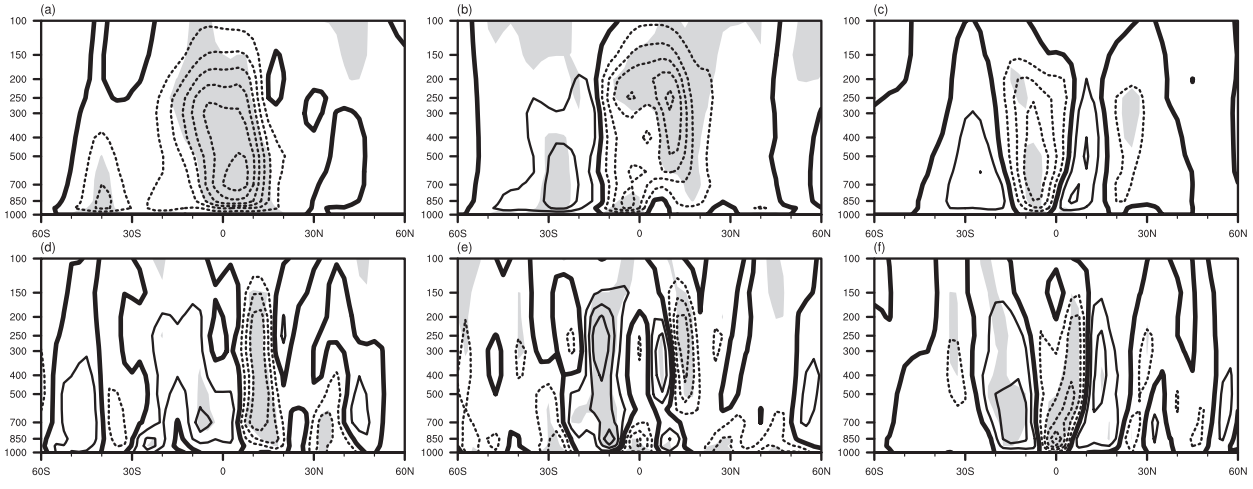

FIG. 7. Regression patterns of the SON MSF with respect to the MASI over the (a) Atlantic sector (10°–60°W), (b) Pacific sector (120°E–90°W), and (c) Indian Ocean sector (40°–110°E). (d)–(f) As in (a)–(c), but for the zonal mean vertical velocity. Period of all regressions is 1950–2010. Shading denotes the regression coefficients exceed the 95% confidence level. Contour intervals are $10^9\,\mathrm{kg\,s^{-1}}$ for (a) and (b) and $4 \times 10^{-4}\,\mathrm{Pa\,s^{-1}}$ for (c) and (d).

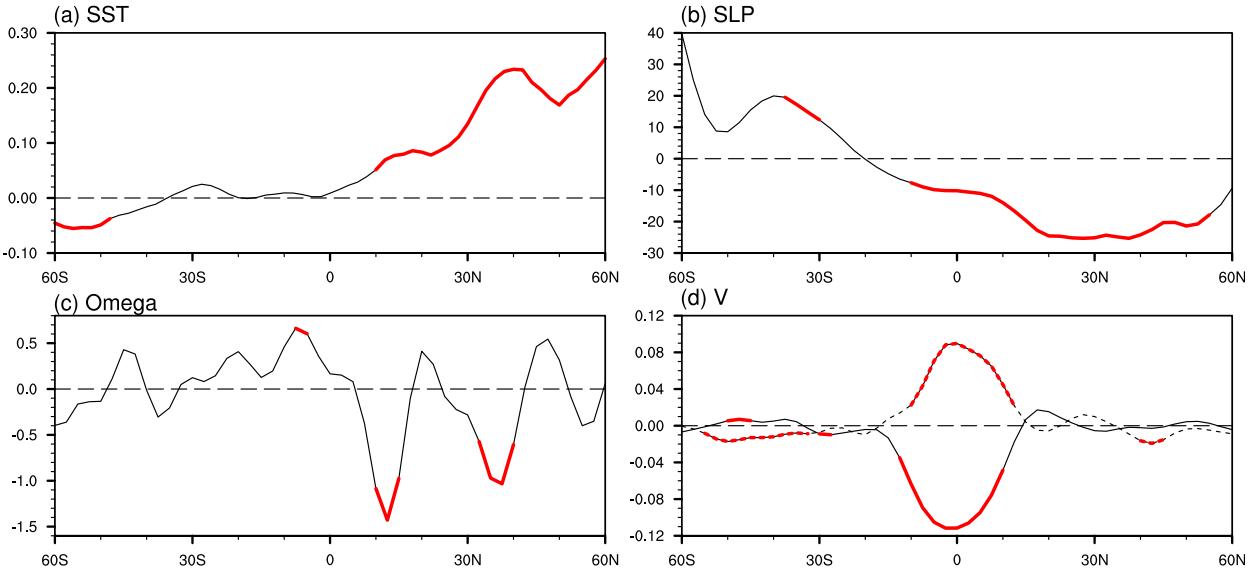

FIG. 8. Zonal mean regression coefficients with respect to AMOI for (a) SSTA, (b) SLP (Pa), (c) vertical velocity at 500 hPa (10^{-3} Pa s^{-1}), and (d) meridional wind (m s^{-1}) at 850 hPa (solid curve) and 100 hPa (dashed curve). The lines highlighted by red color indicate exceeding 90% confidence level.

southern HC boundary extending into the Northern Hemisphere by approximately 10°N, and the southern cell being approximately 25% stronger than the northern cell. The vertical velocity also matches well with the MSF. It shows upward (downward) motion over the deep tropics (subtropics). The strongest upward motion can be observed over the division region of the northern and southern Hadley cells. These results are consistent with observations, indicating good performance of the model. Figures 9b and 9c show the difference of MSF and vertical velocity between E2 and E1 (E2 − E1). The MSF and vertical velocity differences present an equatorially asymmetric cell, with a rising branch located between 10° and 30°N and descending branch near 18°S. Figure 9d shows the difference (E2 − E1) of vertical shear of the zonal mean meridional winds between 200 and 850 hPa. It reaches a minimum at the equator, indicating a strong anomalous cross-equatorial wind, while the climatology of this variable skews to 10°S, corresponding to the climatological MSF (Fig. 9a). The simulated anomalous circulation has similar spatial structure to the AM, indicating a closely relationship between AMO and AM.

Figure 10 shows the differences of the SLP, V100, V850, and w500 between E2 and E1. The SLP difference (Fig. 10a) shows an obvious cross-equatorial gradient. Both V850 and V100 show a strong cross-equatorial meridional wind (Fig. 10b), while w500 shows strong ascending and descending motions over the north and south of the equator, respectively (Fig. 10c). These results are in agreement with the observations (Fig. 8), further confirming that the AMO may play an important role in formation of the AM.

However, there is still difference in the magnitude of the circulation response to AMO between the simulation and the observations. The simulated SLP and vertical and meridional wind are generally larger than the observations. This is mainly because the AMO signal used in the model is larger than two standard deviations, and so the atmospheric response will be stronger than the observations. There are also other factors such as model biases that may affect the circulation response in the simulations. Although the uncertainty exists, the model results can still provide supports for the observational results.

To evaluate the contribution of different ocean basins to the AM, Fig. 11 shows difference of the MSF, vertical velocity, zonally averaged meridional wind shear between the other sensitivity experiments (E3, E4, and E5) and the control experiment (E1). For the MSF, both the Atlantic (E3 − E1) and the Pacific (E4 − E1) experiments show cross-equatorial circulation anomalies (Figs. 11a,d). Strong cross-equatorial vertical shears of the zonal mean meridional wind also can be observed in these two experiments (Figs. 11c,f). The vertical velocity anomaly of E3 − E1 and E4 − E1 show general upward (downward) motion over the Northern (Southern) Hemisphere. These results indicate that both the Atlantic and Pacific Oceans contribute to the formation of the cross-equatorial circulation anomaly. But the

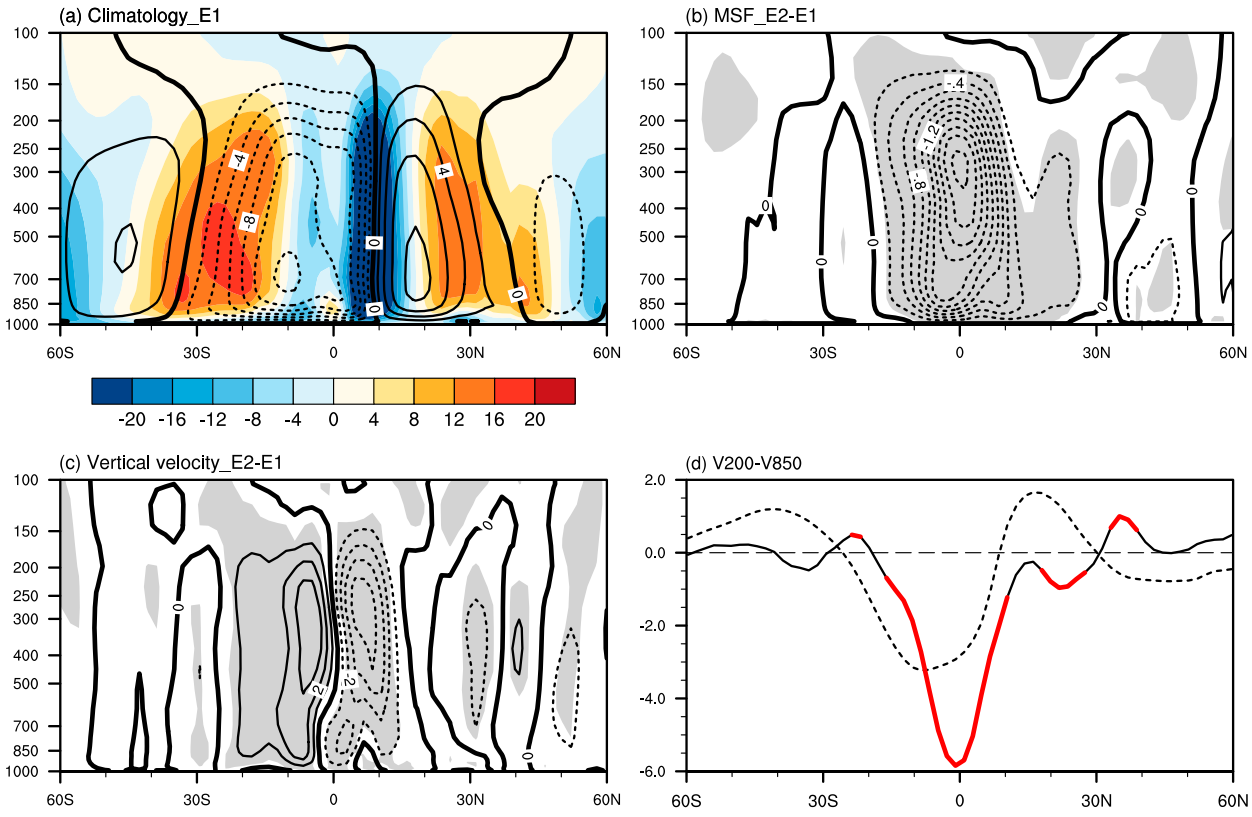

FIG. 9. (a) Climatology of boreal autumn MSF (contours) and vertical velocity (shading) in E1. The difference of the (b) MSF and (c) vertical velocity between E2 and E1. The solid (dashed) contours denote positive (negative) values. The contour intervals are 0.2×10^{10} kg s^{-1} in (b) and 1×10^{-3} Pa s^{-1} in (c). The gray shading indicates where the values exceed 90% confidence level. (d) The zonal mean meridional wind (m s^{-1}) shear between 850 and 200 hPa for the climatology (dashed line) in E1 and the difference between E2 and E1. The difference has been multiplied by a factor of 10 to make its profile more clearly visible in the figure. The red highlighted line indicates exceeding a 90% confidence level.

Atlantic Ocean induces broader latitude coverage of the MSF anomaly than does the Pacific Ocean (Figs. 11a,d). Also, the Atlantic-induced cross-equatorial wind shear is approximately 30% stronger than that of the Pacific Ocean (Figs. 11c,f). These results illustrate that the Atlantic Ocean is the main contributor to the cross-equatorial circulation anomaly.

As to the Indian Ocean (E5 − E1), the significant MSF anomaly is confined to the Northern Hemisphere (Fig. 11g). The vertical shear of the zonal mean meridional wind is symmetric about the equator (Fig. 11i) and strong upward motion is also seen just at the equator. These results indicate that the Indian Ocean has limited influence on the cross-equatorial circulation anomaly.

6. Possible influence on the tropical precipitation

According to the above discussion, the AM favors upward and downward vertical motions over the two hemispheric tropics (e.g., Figs. 5b, 6b, and 9c), and such circulation anomaly changes on multidecadal time scale. The AM may potentially have impacts on the tropical precipitation on multidecadal time scale.

Figure 12a presents the correlation map between AMI and the land precipitation anomaly in SON during the period of 1950–2010. Positive correlation coefficients mainly occur over the lands of Northern Hemisphere, such as North Africa, northern India, the Indo-China Peninsula, and Mexico. Although there are also positive correlation coefficients over South Africa, most lands of the Southern Hemisphere have negative correlations, observed over the mainland of South America, the Maritime Continent, and the mainland of Australia.

In general, the AM has an opposite relationship with Northern and Southern Hemisphere land precipitation. This can be more clearly observed from the zonal mean profile of the correlation coefficients, which shows a dipole pattern with positive and negative correlation coefficients over the Northern and Southern Hemispheres, respectively (Fig. 12a). Moreover, the precipitation

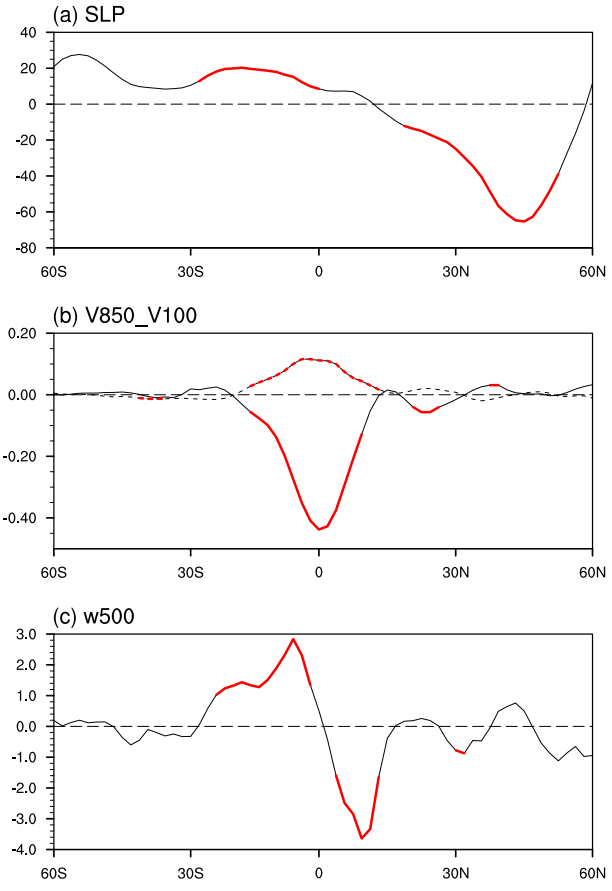

FIG. 10. Zonal mean difference of E2 − E1 for (a) SLP (Pa), (b) meridional wind ($m\,s^{-1}$) at 850 hPa (dashed curve) and 100 hPa (solid curve), and (c) vertical velocity ($10^{-3}\,Pa\,s^{-1}$) at 500 hPa. The lines highlighted by red color indicate exceeding a 90% confidence level.

difference between the northern tropics (NT; 0°–30°N) and the southern tropics (ST; 0°–30°S) shows multidecadal variability (Fig. 12b), which has similar time evolution as the AMI (Fig. 3a). This further suggests that the AM in SON may lead to a seesaw variability of the NT and ST precipitation. Previous studies have also remarked that the interhemispheric temperature gradient has important influence on the tropical precipitation and cross-equatorial energy transport (e.g., Donohoe et al. 2014; Chiang and Friedman 2012; Friedman et al. 2013; Sun et al. 2015a), which is consistent with the results in this study.

7. Summary and discussion

a. Discussion

The HC asymmetric anomaly has been intensively studied. Theoretical study predicts that heating off the equator for several latitude degrees will induce profound asymmetries of the HC anomaly (Lindzen and Hou 1988). This theory have been developed by many subsequent studies (e.g., Walker and Schneider 2006; Fang and Tung 1996, 1997; Adam and Paldor 2010), most of which emphasized the cross-equatorial thermal gradient. Observational studies provide good support for the above theoretical studies. Feng et al. (2013a) shows that the AM in MAM exhibits a long-term trend because of the warming asymmetry between the northern and southern tropical oceans. Feng and Li (2013) also documented that as the warming of the El Niño Modoki is asymmetric about the equator, the HC presents asymmetric responses during the El Niño Modoki event, while the HC shows symmetric response in the canonical El Niño event. These studies focus on the cross-equatorial thermal gradient that originates from the tropics.

The extratropical forcing can also influence the cross-equatorial thermal gradient. Kang et al. (2009) documented that extratropical warming or cooling would give rise to a cross-equatorial heat transport, which is accomplished by inducing a HC asymmetric response. This argument has a lot observation and simulation supports. For example, the slowdown of the Atlantic meridional overturning circulation (AMOC) led to the NH-wide cooling at the end of the 1960s, which is believed to have forced a southward shift of the intertropical convergence zone (ITCZ) over the eastern Pacific and Atlantic (e.g., Alley 2007; Manabe and Stouffer 1988; Chiang and Friedman 2012). The results indicate an asymmetric response of the HC anomaly because the position of the ITCZ coincides with the HC upward branch (e.g., Donohoe et al. 2014).

The AMO is one of the most important extratropical warming or cooling phenomena. It shows warming and cooling of the North Atlantic Ocean with a period of approximately 60 yr (e.g., Enfield et al. 2001; Knight et al. 2005; Sun et al. 2015b,c; Li et al. 2013a,b). It can induce significant cross-equatorial SST and SLP gradients (Fig. 8) and leads to cross-equatorial flow that acts as the lower branch of the asymmetric HC anomaly. The cross-equatorial flow and SST gradient can be both reinforced because of the wind–evaporation–SST (WES) feedback (e.g., Xie and Philander 1994). Additionally, another positive feedback from the convective heating can enhance the asymmetric HC anomaly and the SST pattern (Moura and Shukla 1981).

A study by Friedman et al. (2013) pointed out the interhemispheric temperature asymmetry is an emerging indicator of the global climate change and is closely linked with the asymmetric HC anomaly and the tropical rainfall. They suggest that the AMO is an important

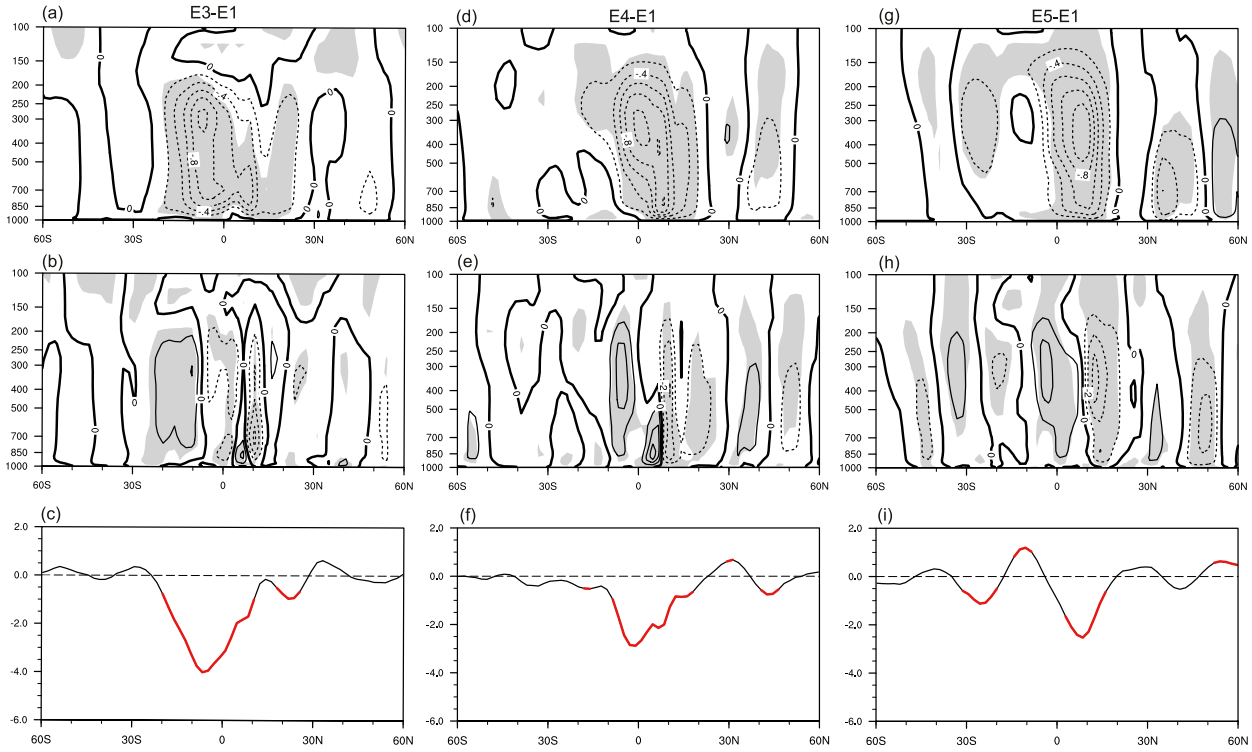

FIG. 11. The differences of the (top) MSF, (middle) vertical velocity, and (bottom) vertical shear of the zonal mean meridional wind for (a)–(c) E3 − E1, (d)–(f) E4 − E1, and (g)–(i) E5 − E1. Units for MSF, vertical velocity, and vertical shear of the zonal mean meridional wind are 10^{10} kg s^{-1}, 10^{-3} Pa s^{-1}, and m s^{-1}. The contour intervals in (a),(d), and (g) are 0.2×10^{10} kg s^{-1}, and in (b),(e), and (f) are 1×10^{-3} Pa s^{-1}. The gray shading indicates where the values exceed 90% confidence level. The values in (c) have been multiplied by a factor of 10 for ease of comparison. The red lines indicate where the values exceed 90% confidence level.

factor that can influence the interhemispheric temperature asymmetry on multidecadal time scales. Therefore, it dominates the multidecadal variability of the AM and the southern and northern tropical rainfall difference. To figure out how much AMO contributes to the HC variability, Fig. 13 shows the explained variance of HC by AMO in each season. The explained variance in SON ranges from 5% to 50% in the tropics, which presents an AM-like distribution, indicating that the AMO relates closely to the asymmetric component of the HC. In JJA, the explained variance also displays an AM-like distribution but is much smaller (5%–20%) than that in SON. In MAM and DJF, the explained variances in the tropics are small (less than 15%) and no AM-like pattern is observed. It means that the explained variance of HC by AMO varies spatially and temporally. The largest explained variance occurs in SON and the second largest in JJA. In SON, the largest explained variance is at the low-level troposphere (700 hPa). The results also imply that the AMO in SON may have a unique feature that is different from the other seasons.

Another interesting question is why AMs in the other three seasons do not show multidecadal variability. Table 1 displays the correlation coefficients between the AMI and MASI, the detrended MASI, and the AMOI in four seasons, respectively. The AMI and the MASI have consistent correlation throughout the four seasons. But the correlation may be due to different causes. Previous studies suggested that AMs in MAM, JJA, and DJF are closely related to the decadal warming of the Indo-Pacific warm pool (e.g., Ma and Li 2008; Feng et al. 2011, 2013). If we remove the linear trends of the MASI in all four seasons, the correlation coefficients decrease in MAM, JJA and DJF, whereas they are almost unchanged in SON (Table 1). The results imply that the correlation between AMI and MASI in SON is not due to the long-term trend of the MASI. The correlation between AMI and AMOI in SON (R = 0.57) is much larger than those in the other seasons, indicating that the AMO in SON has unique impact on the AM.

If we regress the zonal mean SSTA onto the AMOI, the regressed SSTA at the equator displays warm centers in MAM and DJF. Given that the climatological SST is warmer at the equator than the off-equatorial region, the SSTA peaks at the equator may induce upward motion around the equator, which can be observed through the AMOI regressed zonal mean vertical velocity at 500 hPa. But in SON, the regressed SSTA

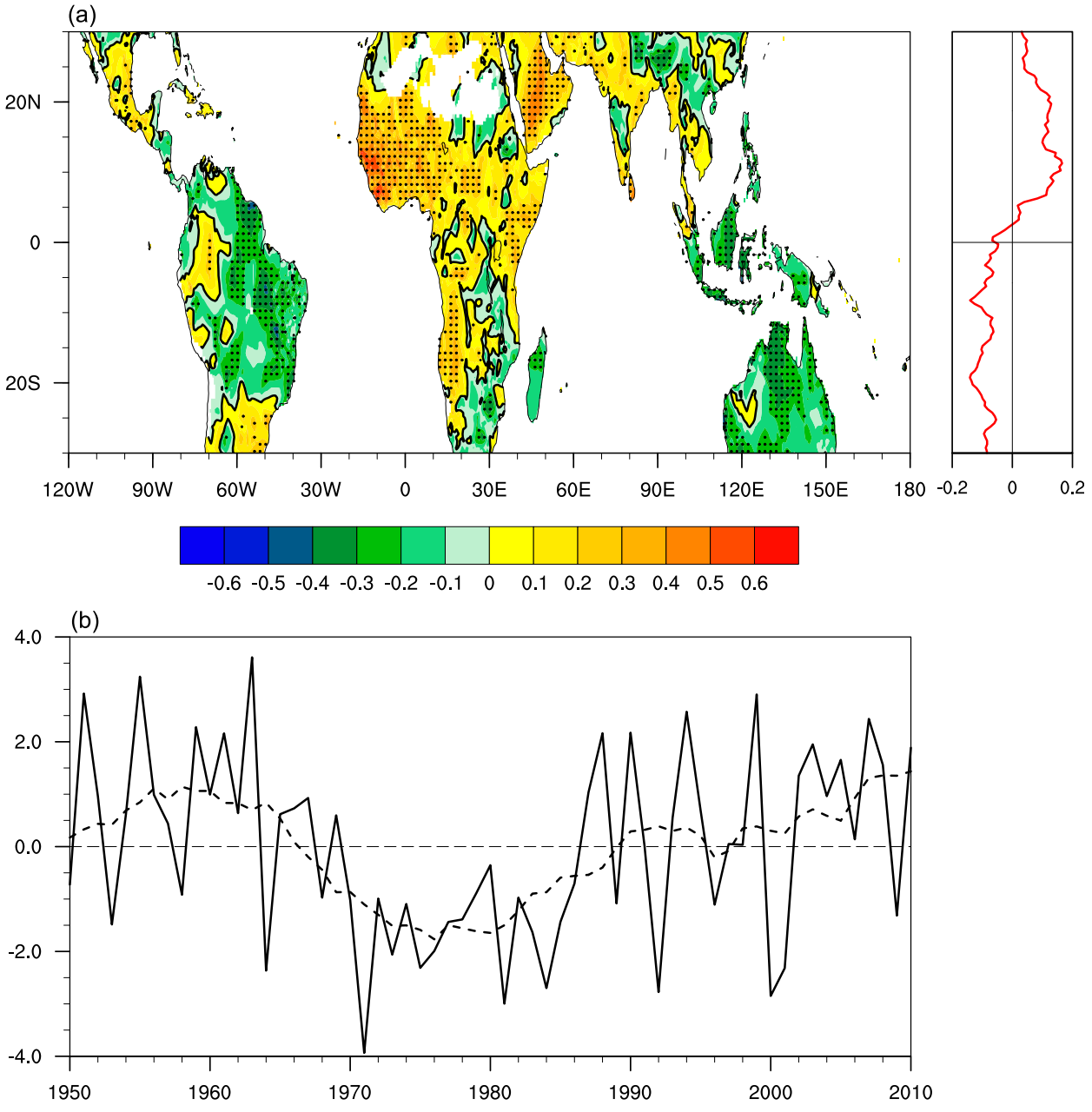

FIG. 12. (a) Correlation map between AMI and the tropical (30°S–30°N) land precipitation in SON, during the period of 1950–2010. Correlation of the zonal mean land precipitation with the AMI is shown as the red line on the right panel. Black contours denote the zero line, and dot marked areas are significant above 90% confidence level. (b) Time series of the boreal autumn land precipitation difference (solid line) between the NT and ST (NT minus ST) during the period of 1950–2010, and its 11-yr running mean (dashed line). NT: 0°–30°N, ST: 0°–30°S.

shows a large cross-equatorial gradient yet nearly no warming at the equator; this would induce off-equatorial upward motion in the Northern Hemisphere, which is observed through the regressed vertical velocity. Held and Hou (1980) also suggest that the off-equatorial heating can induce an AM-like HC anomaly. In JJA, the SSTA profile matches well with that in SON, but there is anomalous warming in the southern tropics (0°–20°S), which weakens the cross-equatorial SST gradient. Thus, the Northern Hemisphere off-equatorial upward motion is only about half of that in SON. This result is also consistent with those in Figs. 13b and 13c, in which the explained variance of HC by AMO in JJA is similar to that in SON, but is much smaller. There are also

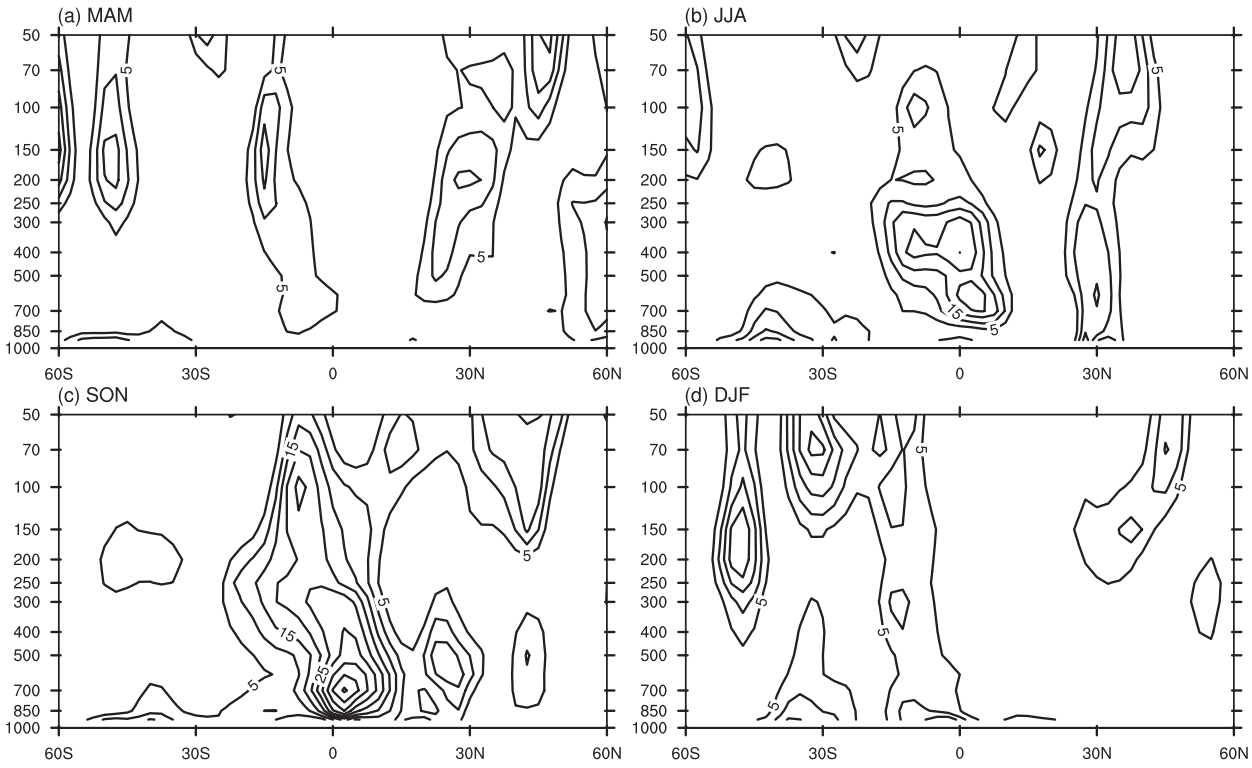

FIG. 13. Latitude–pressure sections of the explained variance (the square of correlation coefficients between AMOI and the MSF; units: %) of the HC by AMO in (a) MAM, (b) JJA, (c) SON and (d) DJF, respectively.

studies addressing the idea that the AMO in SON has special climate impacts. Goswami et al. (2006) pointed out that the AMO in boreal late summer and autumn induces a strong meridional tropospheric temperature gradient, which can impact the Indian summer monsoon rainfall.

More evidence can be found through numerical simulation. When the AMO-related SSTA is imposed throughout the seasons with CAM5, in the same manner as in SON, the asymmetry and strength of the circulation response in MAM, JJA, and DJF is much weaker than that in SON; among these MAM is the weakest (figure not shown). The model simulation results are consistent with the observational analysis, also suggesting the unique impact of boreal autumn AMO on HC.

As to the formation of the SST pattern, involving complex processes of air–sea interaction, we hope to explore these issues in the future work. The present study can also promote our understanding of the HC variability and the influences on the tropical climate. But the underlying dynamical mechanisms still need further study.

b. Summary

Previous studies have demonstrated that the variability of HC in MAM, JJA, and DJF is dominated by two modes, the AM and SM. The AM shows a long-term trend that is closely linked to the Indo-Pacific Warm Pool (IPWP) warming. The SM shows interannual variability that is related to the ENSO (e.g., Ma and Li 2008; Feng et al. 2011, 2013). In this study, we focus on the HC variability in boreal autumn, which has been less prominent in previous studies. We found that the HC variability in SON is also dominated by an AM that has an explained variance of approximately 40%. It shows obvious multidecadal variability, unlike the other three seasons. The multidecadal variability of AM is closely related to the AMO. Further analysis demonstrates that in MAM and DJF the AMO is associated with anomalous warming at the equator, which failed to induce asymmetric circulation anomaly. In JJA, the cross-equatorial SST gradient is smaller in SON, resulting in a much weaker asymmetric circulation anomaly. We also found that the AM in SON has close relationship with the tropical land precipitation. The AMI has reversed correlation with the land precipitation between NT and ST. The precipitation difference between NT and ST also shows robust multidecadal variability.

Acknowledgments. We thank the editor and the three anonymous referees, whose comments improved the

paper. This work was jointly supported by the National Natural Science Foundation of China (41530424 and 41475076).

REFERENCES

Adam, O., and N. Paldor, 2010: Global circulation in an axially symmetric shallow-water model, forced by off-equatorial differential heating. *J. Atmos. Sci.*, **67**, 1275–1286, doi:10.1175/2009JAS3324.1.

Alley, R. B., 2007: Wally was right: Predictive ability of the North Atlantic "conveyor belt" hypothesis for abrupt climate change. *Annu. Rev. Earth Planet. Sci.*, **35**, 241–272, doi:10.1146/annurev.earth.35.081006.131524.

Chang, E. K. M., 1995: The influence of Hadley circulation intensity changes on extratropical climate in an idealized model. *J. Atmos. Sci.*, **52**, 2006–2024, doi:10.1175/1520-0469(1995)052<2006:TIOHCI>2.0.CO;2.

Chen, J. Y., B. E. Carlson, and A. D. Del Genio, 2002: Evidence for strengthening of the tropical general circulation in the 1990s. *Science*, **295**, 838–841, doi:10.1126/science.1065835.

Chiang, J. C. H., and A. R. Friedman, 2012: Extratropical cooling, interhemispheric thermal gradients, and tropical climate change. *Annu. Rev. Earth Planet. Sci.*, **40**, 383–412, doi:10.1146/annurev-earth-042711-105545.

Compo, G. P., and Coauthors, 2011: The Twentieth Century Reanalysis Project. *Quart. J. Roy. Meteor. Soc.*, **137**, 1–28, doi:10.1002/qj.776.

Dee, D. P., and Coauthors, 2011: The ERA-Interim reanalysis: Configuration and performance of the data assimilation system. *Quart. J. Roy. Meteor. Soc.*, **137**, 553–597, doi:10.1002/qj.828.

Diaz, H. F., and B. Bradley, 2004: *The Hadley Circulation: Present, Past and Future*. Kluwer Academic, 511 pp.

Dima, I. M., and J. M. Wallace, 2003: On the seasonality of the Hadley cell. *J. Atmos. Sci.*, **60**, 1522–1527, doi:10.1175/1520-0469(2003)060<1522:OTSOTH>2.0.CO;2.

Donohoe, A., J. Marshall, D. Ferreira, K. Armour, and D. McGee, 2014: The interannual variability of tropical precipitation and interhemispheric energy transport. *J. Climate*, **27**, 3377–3392, doi:10.1175/JCLI-D-13-00499.1.

Enfield, D. B., A. M. Mestas-Nuñez, and P. J. Trimble, 2001: The Atlantic multidecadal oscillation and its relation to rainfall and river flows in the continental U.S. *Geophys. Res. Lett.*, **28**, 2077–2080, doi:10.1029/2000GL012745.

Fang, M., and K. K. Tung, 1996: A simple model of nonlinear Hadley circulation with an ITCZ: Analytic and numerical solutions. *J. Atmos. Sci.*, **53**, 1241–1261, doi:10.1175/1520-0469(1996)053<1241:ASMONH>2.0.CO;2.

——, and ——, 1997: The dependence of the Hadley circulation on the thermal relaxation time. *J. Atmos. Sci.*, **54**, 1379–1384, doi:10.1175/1520-0469(1997)054<1379:TDOTHC>2.0.CO;2.

Feng, J., and J. P. Li, 2013: Contrasting impacts of two types of ENSO on the boreal spring Hadley circulation. *J. Climate*, **26**, 4773–4789, doi:10.1175/JCLI-D-12-00298.1.

——, ——, and F. Xie, 2013: Long-term variation of the principal mode of boreal spring Hadley circulation linked to SST over the Indo-Pacific warm pool. *J. Climate*, **26**, 532–544, doi:10.1175/JCLI-D-12-00066.1.

Feng, R., J. P. Li, and J. C. Wang, 2011: Regime change of the boreal summer Hadley circulation and its connection with the tropical SST. *J. Climate*, **24**, 3867–3877, doi:10.1175/2011JCLI3959.1.

Friedman, A. R., Y. T. Hwang, J. C. H. Chiang, and D. M. W. Frierson, 2013: Interhemispheric temperature asymmetry over the twentieth century and in future projections. *J. Climate*, **26**, 5419–5433, doi:10.1175/JCLI-D-12-00525.1.

Frierson, D. M. W., J. Lu, and G. Chen, 2007: Width of the Hadley cell in simple and comprehensive general circulation models. *Geophys. Res. Lett.*, **34**, L18804, doi:10.1029/2007GL031115.

Fu, Q., C. M. Johanson, J. M. Wallace, and T. Reichler, 2006: Enhanced mid-latitude tropospheric warming in satellite measurements. *Science*, **312**, 1179, doi:10.1126/science.1125566.

Goswami, B. N., M. S. Madhusoodanan, C. P. Neema, and D. Sengupta, 2006: A physical mechanism for North Atlantic SST influence on the Indian summer monsoon. *Geophys. Res. Lett.*, **33**, L02706, doi:10.1029/2005GL024803.

Held, I. M., and A. Y. Hou, 1980: Nonlinear axially symmetric circulations in a nearly inviscid atmosphere. *J. Atmos. Sci.*, **37**, 515–533, doi:10.1175/1520-0469(1980)037<0515:NASCIA>2.0.CO;2.

——, and B. J. Soden, 2006: Robust responses of the hydrological cycle to global warming. *J. Climate*, **19**, 5686–5699, doi:10.1175/JCLI3990.1.

Holton, J. R., 1992: *An Introduction to Dynamic Meteorology*. 3rd ed. Academic Press, 511 pp.

Hou, A. Y., 1998: Hadley circulation as a modulator of the extratropical climate. *J. Climate*, **55**, 2437–2457, doi:10.1175/1520-0469(1998)055<2437:HCAAMO>2.0.CO;2.

Hu, D. Z., W. S. Tian, F. Xie, J. C. Shu, and S. Dhomse, 2014: Effects of meridional sea surface temperature changes on stratospheric temperature and circulation. *Adv. Atmos. Sci.*, **31**, 888–900, doi:10.1007/s00376-013-3152-6.

Hu, Y., and Q. Fu, 2007: Observed poleward expansion of the Hadley circulation since 1979. *Atmos. Chem. Phys.*, **7**, 5229–5236, doi:10.5194/acp-7-5229-2007.

——, K. K. Tung, and J. Liu, 2005: A closer comparison of early and late winter atmospheric trends in the Northern Hemisphere. *J. Climate*, **18**, 3204–3216, doi:10.1175/JCLI3468.1.

Johanson, C. M., and Q. Fu, 2009: Hadley cell widening: Model simulations versus observations. *J. Climate*, **22**, 2713–2725, doi:10.1175/2008JCLI2620.1.

Kalnay, E., and Coauthors, 1996: The NCEP/NCAR 40-Year Reanalysis Project. *Bull. Amer. Meteor. Soc.*, **77**, 437–471, doi:10.1175/1520-0477(1996)077<0437:TNYRP>2.0.CO;2.

Kanamitsu, M., W. Ebisuzaki, J. Woollen, S.-K. Yang, J. J. Hnilo, M. Fiorino, and G. L. Potter, 2002: NCEP–DOE AMIP-II Reanalysis (R-2). *Bull. Amer. Meteor. Soc.*, **83**, 1631–1643, doi:10.1175/BAMS-83-11-1631.

Kang, S. M., D. M. W. Frierson, and I. M. Held, 2009: The tropical response to extratropical thermal forcing in an idealized GCM: The importance of radiative feedbacks and convective parameterization. *J. Atmos. Sci.*, **66**, 2812–2827, doi:10.1175/2009JAS2924.1.

Knight, J. R., R. J. Allan, C. K. Folland, M. Vellinga, and M. E. Mann, 2005: A signature of persistent natural thermohaline circulation cycles in observed climate. *Geophys. Res. Lett.*, **32**, L20708, doi:10.1029/2005GL024233.

Li, J. P., 2001: *Atlas of Climate of Global Atmospheric Circulation I* (in Chinese). China Meteorology Press, 279 pp.

——, and Coauthors, 2013a: Progress in air–land–sea interactions in Asia and their role in global and Asian climate change (in Chinese). *Chin. J. Atmos. Sci.*, **37**, 518–538.

——, C. Sun, and F.-F. Jin, 2013b: NAO implicated as a predictor of Northern Hemisphere mean temperature multidecadal

variability. *Geophys. Res. Lett.*, **40**, 5497–5502, doi:10.1002/2013GL057877.

Li, Y., J. P. Li, and J. Feng, 2012: A teleconnection between the reduction of rainfall in southwest western Australia and north China. *J. Climate*, **25**, 8444–8461, doi:10.1175/JCLI-D-11-00613.1.

Lindzen, R. S., 1994: Climate dynamics and global change. *Annu. Rev. Fluid Mech.*, **26**, 353–378, doi:10.1146/annurev.fl.26.010194.002033.

——, and A. Y. Hou, 1988: Hadley circulations for zonally averaged heating centered off the equator. *J. Atmos. Sci.*, **45**, 2416–2427, doi:10.1175/1520-0469(1988)045<2416:HCFZAH>2.0.CO;2.

Lu, J., G. A. Vecchi, and T. Reichler, 2007: Expansion of the Hadley cell under global warming. *Geophys. Res. Lett.*, **34**, L06805, doi:10.1029/2006GL028443.

Ma, J., and J. Li, 2007: Strengthening of the boreal winter Hadley circulation and its connection with ENSO. *Prog. Nat. Sci.*, **17**, 1327–1333.

——, and ——, 2008: The principal modes of variability of the boreal winter Hadley cell. *Geophys. Res. Lett.*, **35**, L01808, doi:10.1029/2007GL031883.

Manabe, S., and R. J. Stouffer, 1988: Two stable equilibria of a coupled ocean–atmosphere model. *J. Climate*, **1**, 841–866, doi:10.1175/1520-0442(1988)001<0841:TSEOAC>2.0.CO;2.

Mantsis, D. F., and A. C. Clement, 2009: Simulated variability in the mean atmospheric meridional circulation over the 20th century. *Geophys. Res. Lett.*, **36**, L06704, doi:10.1029/2008GL036741.

Mitas, C. M., and A. Clement, 2005: Has the Hadley cell been strengthening in recent decades? *Geophys. Res. Lett.*, **32**, L03809, doi:10.1029/2004GL021765.

——, and ——, 2006: Recent behavior of the Hadley cell and tropical thermodynamics in climate models and reanalyses. *Geophys. Res. Lett.*, **33**, L01810, doi:10.1029/2005GL024406.

Mitchell, T. D., and P. D. Jones, 2005: An improved method of constructing a database of monthly climate observations and associated high-resolution grids. *Int. J. Climatol.*, **25**, 693–712, doi:10.1002/joc.1181.

Moura, A. D., and J. Shukla, 1981: On the dynamics of droughts in Northeast Brazil: Observations, theory and numerical experiments with a general circulation model. *J. Atmos. Sci.*, **38**, 2653–2675, doi:10.1175/1520-0469(1981)038<2653:OTDODI>2.0.CO;2.

Onogi, K., and Coauthors, 2005: JRA-25: Japanese 25-Year Reanalysis Project—Progress and status. *Quart. J. Roy. Meteor. Soc.*, **131**, 3259–3268, doi:10.1256/qj.05.88.

Parker, D., C. Folland, A. Scaife, J. Knight, A. Colman, P. Baines, and B. Dong, 2007: Decadal to multidecadal variability and the climate change background. *J. Geophys. Res.*, **112**, D18115, doi:10.1029/2007JD008411.

Quan, X. W., H. F. Diaz, and M. P. Hoerling, 2004: Change in the tropical Hadley cell since 1950. *The Hadley Circulation: Past, Present, and Future*, H. F. Diaz and R. S. Bradley, Eds., Cambridge University Press, 85–120.

Rienecker, M. M., and Coauthors, 2011: MERRA: NASA's Modern-Era Retrospective analysis for research and applications. *J. Climate*, **24**, 3624–3648, doi:10.1175/JCLI-D-11-00015.1.

Saha, S., and Coauthors, 2010: The NCEP Climate Forecast System Reanalysis. *Bull. Amer. Meteor. Soc.*, **91**, 1015–1057, doi:10.1175/2010BAMS3001.1.

Santer, B. D., and Coauthors, 2005: Amplification of surface temperature trends and variability in the tropical atmosphere. *Science*, **309**, 1551–1556, doi:10.1126/science.1114867.

Smith, T. M., R. W. Reynolds, T. C. Peterson, and J. Lawrimore, 2008: Improvements to NOAA's historical merged land–ocean surface temperature analysis (1880–2006). *J. Climate*, **21**, 2283–2296, doi:10.1175/2007JCLI2100.1.

Sun, C., J. Li, F.-F. Jin, and R. Ding, 2013: Sea surface temperature inter-hemispheric dipole and its relation to tropical precipitation. *Environ. Res. Lett.*, **8**, 044006, doi:10.1088/1748-9326/8/4/044006.

——, ——, J. Feng, and F. Xie, 2015a: A decadal-scale teleconnection between the North Atlantic Oscillation and subtropical eastern Australian rainfall. *J. Climate*, **28**, 1074–1092, doi:10.1175/JCLI-D-14-00372.1.

——, ——, and F.-F. Jin, 2015b: A delayed oscillator model for the quasi-periodic multidecadal variability of the NAO. *Climate Dyn.*, **45**, 2083–2099, doi:10.1007/s00382-014-2459-z.

——, ——, and S. Zhao, 2015c: Remote influence of Atlantic multidecadal variability on Siberian warm season precipitation. *Sci. Rep.*, **5**, 16853, doi:10.1038/srep16853.

Sun, Y., and T. J. Zhou, 2014: How does El Niño affect the interannual variability of the boreal summer Hadley circulation? *J. Climate*, **27**, 2622–2642, doi:10.1175/JCLI-D-13-00277.1.

Tanaka, H. L., N. Ishizaki, and A. Kitoh, 2004: Trend and interannual variability of Walker, monsoon and Hadley circulations defined by velocity potential in the upper troposphere. *Tellus*, **56A**, 250–269, doi:10.1111/j.1600-0870.2004.00049.x.

Uppala, S. M., and Coauthors, 2005: The ERA-40 Re-Analysis. *Quart. J. Roy. Meteor. Soc.*, **131**, 2961–3012, doi:10.1256/qj.04.176.

Walker, C. C., and T. Schneider, 2006: Eddy influences on Hadley circulations: Simulations with an idealized GCM. *J. Atmos. Sci.*, **63**, 3333–3350, doi:10.1175/JAS3821.1.

Wielicki, B. A., and Coauthors, 2002: Evidence for large decadal variability in the tropical mean radiative energy budget. *Science*, **295**, 841–844, doi:10.1126/science.1065837.

Xie, S. P., and S. G. H. Philander, 1994: A coupled ocean–atmosphere model of relevance to the ITCZ in the eastern Pacific. *Tellus*, **46A**, 340–350, doi:10.1034/j.1600-0870.1994.t01-1-00001.x.

Zhan, R.-F., Y. Wang, and M. Wen, 2013: The SST gradient between the southwest Pacific and the western Pacific warm pool: A new factor controlling the northwestern Pacific tropical cyclone genesis frequency. *J. Climate*, **26**, 2408–2415, doi:10.1175/JCLI-D-12-00798.1.

Zhao, H. X., and G. W. K. Moore, 2008: Trends in the boreal summer regional Hadley and Walker circulations as expressed in precipitation records from Asia and Africa during the latter half of the 20th century. *Int. J. Climatol.*, **28**, 563–578, doi:10.1002/joc.1580.